Computers and Geotechnics 137 (2021) 104259

Contents lists available at ScienceDirect

Computers and Geotechnics

journal homepage: www.elsevier.com/locate/compgeo

Mesoscale numerical investigation of the effects of fiber stiffness on the shear behavior of fiber-reinforced granular soil

Ningyu Yang [a], Xiaobin Chen [a,*], Ruidong Li [a], Junqi Zhang [b,*], Hang Hu [a], Jiasheng Zhang [a]

[a] School of Civil Engineering, Central South University, Changsha, Hunan 410083, China
[b] College of Water Resources and Civil Engineering, Hunan Agricultural University, Changsha, Hunan 410128, China

ARTICLE INFO

Keywords:
Fiber-reinforced soil
Shear behavior
Discrete element method
Fiber stiffness
Micromechanical properties

ABSTRACT

Fiber reinforcement techniques can effectively optimize the engineering properties of ground soils. This study aims to investigate the influence of fiber stiffness on the shear behavior of fiber-reinforced granular soil. First, the particle shapes are automatically extracted based on the improved Viola–Jones algorithm. Subsequently, the fiber stiffness is calibrated considering the results of laboratory tensile tests. Moreover, a series of numerical biaxial tests are conducted considering different fiber stiffnesses and contents and a flexible boundary. The influence of the fiber stiffness on the strength and volumetric strain is analyzed, and the stress–dilatancy relationship of the fiber-reinforced soil is discussed. In addition, the interaction between the fibers and soil particles is clarified according to the internal structure and stress network, including the coordination number, contribution of the contact, sliding of the particles and mobilization of the tensile force in the fibers. The results of this study can help clarify the reinforcement mechanism of fibers with typical stiffness values.

1. Introduction

Soil reinforcement has been widely used in the field of geotechnical engineering to enhance the soil strength and stabilization of the ground soil (Botero et al., 2015; Diambra et al., 2013; Jamshidi Chenari et al., 2016). Common reinforcement geosynthetics, such as geotextiles, geogrids and fibers, have been proven to be efficient (Botero et al., 2015). In comparison with geotextiles and geomembranes, fibers can easily mix with soil to generate random and uniform distributions and avoid the formation of potentially weak structural planes (Ling et al., 1994; Wang et al., 2014). In recent years, fiber-reinforced soils have been successfully used to increase the stability of slopes and perform ground improvement for foundations and subgrades (Naderi and Hataf, 2014; Santoni et al., 2001; Sharma and Kumar, 2019). Therefore, the engineering behaviors of fiber-reinforced soil are of considerable interest to geotechnical engineering researchers and practitioners.

Many experimental studies utilizing triaxial tests, unconfined compression tests, and direct shear tests have been conducted to investigate the mechanical properties of fiber-reinforced granular soil (Patel and Singh, 2019; Sadek et al., 2010; Yetimoglu and Salbas, 2003). In the context of traditional fiber-reinforced soil, researchers have focused on the effects of the fiber content (FC), type of fiber, shape of granular soils and fiber orientations on the strength and deformation characteristics of fiber-reinforced soil (Al-Refeai, 1991; Gong et al., 2020; Gray and Al-Refeai, 1986; Michalowski and Čermák, 2003). In recent years, with the use of fibers increase, waste tire rubber chips, waste plastic bags and other low-stiffness materials (Akbarimehr et al., 2020) have been considered fibers and used to enhance the engineering properties of soil. The reinforcement mechanisms of low-stiffness and traditional (high stiffness) fibers are different. However, only a few investigations have been conducted to clarify the effect of the fiber stiffness on the properties of fiber-reinforced soil. With the development of the discrete element method (DEM), many investigations have been performed to explain the mechanisms of the mechanical behaviors in laboratory experiments (Gong and Liu, 2015; Wang et al., 2019) and engineering problems (Jiang and Yin, 2014; Wang and Yin, 2020) by using the DEM and adopting new methods to obtain the soil parameters (Jin et al., 2017; 2016). Several scholars explored the mechanism of fiber reinforcement by using the DEM (Gong et al., 2020); however, in the existing DEM models, the particle shapes were ignored, and rigid walls were considered as the boundary conditions. Nevertheless, the existing research has demonstrated that the particle shapes considerably influence the soil properties, including the shear behavior and particle breakage (Jin et al., 2018; Wang et al., 2021; Yin et al., 2020), and the

* Corresponding authors.
E-mail addresses: chen_xiaobin@csu.edu.cn (X. Chen), zjq1990@csu.edu.cn (J. Zhang).

https://doi.org/10.1016/j.compgeo.2021.104259
Received 20 January 2021; Received in revised form 30 April 2021; Accepted 15 May 2021
Available online 10 June 2021

boundary conditions affect the volumetric change and failure mode of the samples (Qu et al., 2019).

To fill these gaps, the effects of the fiber stiffness and FC on the shear behaviors of fiber-reinforced soil are quantitatively investigated using the DEM framework. First, the particle shape is extracted, and a database of the soil particle shapes is built based on the improved Viola–Jones algorithm. Subsequently, the fiber parameters are calibrated according to tensile testing, and a series of numerical biaxial tests are conducted using different fiber stiffnesses and contents. The numerical samples with different stiffness fibers have the same initial fabric, and the confining pressure is applied using a flexible boundary. The results of numerical tests are comprehensively analyzed considering the stress in the fibers, internal structure and stress network. In addition, the differences in the reinforcement mechanisms of high-stiffness and low-stiffness fibers in soils are evaluated. The results of this study can help clarify the reinforcement mechanism of fibers with typical stiffness values.

2. Materials

2.1. Automated extraction of soil particles

The improved Viola–Jones algorithm (Viola, 2001) is used to automatically identify the shape of typical granular soil (standard sands). The photograph of a sample is shown in Fig. 1. The whole process is divided into four main steps: (1) marking of the images to create the training data set, as shown in Fig. 2(a). The images containing a complete outline of the filler particles are labeled as positive images, whereas the remaining images are labeled as negative images. (2) Rotating and scaling of the training set images, as shown in Fig. 2(b) and 2(c). Rotating is implemented because certain particles are aslant, and the sliding windows may not be able to detect these particles. Scaling is performed to expand the dataset to consider particles having certain potential shapes. (3) Training of the model by using the Adaboost and Cascade methods (Islam et al., 2008). (4) Sand particle recognition based on the sliding window method, as shown in Fig. 3. First, a 30 × 30 sliding window is applied to scan the whole image. In each window, the image is cropped as the input to the classifier in the cascade method. If the output is positive, the image is moved to stage 2 in the cascade method. Otherwise, the negative image is rejected, and the sliding window moves to the next position corresponding to a shift of 1 pixel. If the cropped image successfully passes all the classifiers, the image is highly likely a positive image containing a full-projection particle. The sliding window at this position is marked as a bounding box of this particle. Next, the sliding window is continually moved in increments of 1 pixel in both the horizontal and vertical directions. The movement path is shown in Fig. 3. When the 30 × 30 sliding window successfully scans the whole image, the size of the sliding window is increased by 10 pixels in both directions, as shown in Fig. 3. The sliding procedure is repeated until the sliding window is expanded to a maximum size of 100 × 100 pixels.

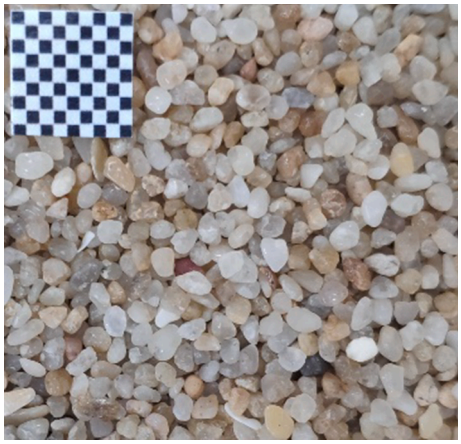

Fig. 1. Image of the sand sample.

After the sand particles with complete contours are identified, a series of geometric algorithms are used to calculate the shape parameters of the particles. The shape of the particles is described by three geometric shape evaluation indexes: elongation, roundness and roughness.

The elongation, *EI*, can be defined as follows:

$$EI = S/L \tag{1}$$

where S and L are the particle dimensions in the direction of the minimum and maximum principal axes, respectively. For an ideal round or equilateral polygonal particle, *EI* is 1.

The roundness, *Rd*, describes the degree to which the edges and corners on a particle's surface mimic a circle:

$$Rd = \frac{\sum R_c}{n_c R_{insc}} \tag{2}$$

where R_{insc} is the radius of the largest inscribed circle, R_c is the radius of the circumscribed circle located at the center of the particle, and n_c is the number of angular regions.

The roughness, *Rg*, reflects the shape irregularity superimposed on the grain surface corner and can be calculated as follows. First, the particle profile is decomposed. Thus, 2D particles are expanded to continuous points corresponding to θ and d according to the angle θ and polarity diameter$d$ in the polarity system.

Next, the discrete points are transformed into a smooth curve/surface using the local weighted regression smoothing (LOESS) method, and the following formula is obtained:

$$Rg = \sqrt{\frac{1}{n}\sum_{i=1}^{n}\left(y_i - y_{i-LOESS}\right)^2} \tag{3}$$

where n is the number of points on the 2D particle contour, y_i is the y-coordinate of point i, and $y_{i-LOESS}$ is the Y-axis coordinate of point i after smoothing.

To facilitate the preparation of sand particle samples with real shapes in terms of the discrete elements, a sand particle model library is established. In particular, as shown in Table 1, the shape index of the sand particles is stored together with the contour coordinates in the following format: [digital, contour, elongation, roundness, roughness]. The following steps are adopted to import the contours of the sand particles into the discrete element software. (1) First, the range of sand particle shape parameters is input. (2) Next, according to the range of these values, the 2D sand particle contour that meets the requirements is automatically searched. (3) Finally, the 2D sand particle contour is output as a "DXF" file and transformed into the clump particle model in PFC2D 5.0 software through the command flow written by the FISH.

After establishing the particle library, 2D profiles of the sand particles satisfying specific requirements can be selected to facilitate the discrete element modeling of the fiber–soil mixture with real particle shapes, thus laying a foundation to consider the geometry of real soil particles in subsequent modeling. The particle shapes are used to generate soil particles, and the index is as presented in Table 1.

2.2. Fiber parameters

According to the definition of the fibers proposed by Ajayi et al. (2017), the fiber length is selected to be 12 mm (7.1 times the average particle diameter), and the particle diameter of the granular soil is 1–2 mm (uniform distribution), consistent with that in the previous investigation of the fiber-reinforced soil (Gong et al., 2020). The fiber consists of 36 balls, and the distance between the centers of the two adjacent bonded balls is 0.72 times the ball diameter. The fiber stiffness is

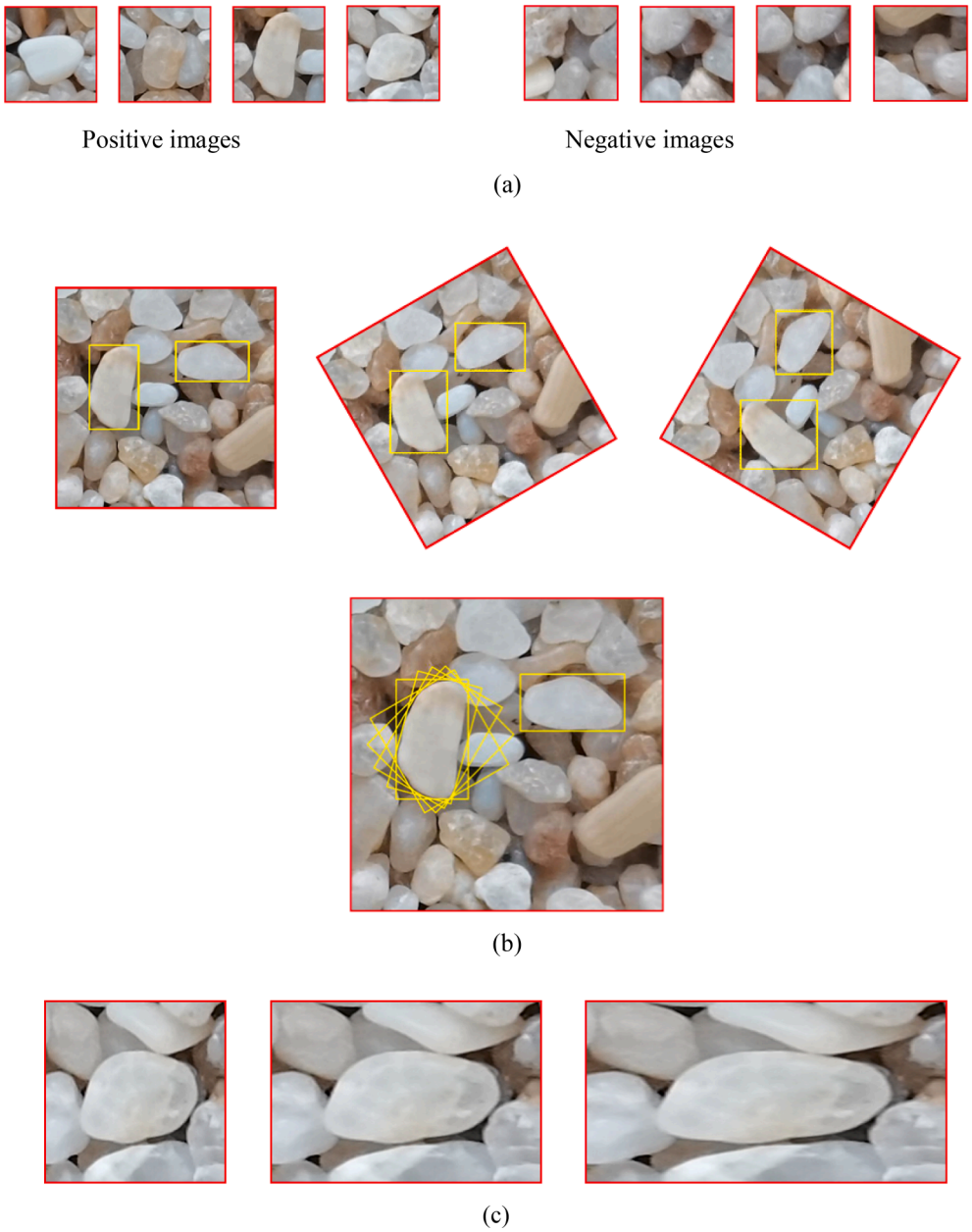

Fig. 2. Image processing: (a) marking of the images, and (b) rotation and (c) scaling of the training set images.

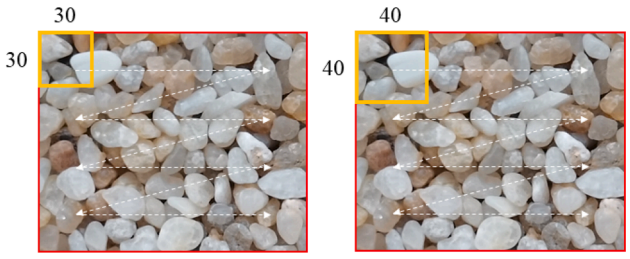

Fig. 3. Sliding window method.

calculated by summarizing the stiffness values of different fibers used in fiber-reinforced soil. In general, the fibers with a high stiffness have received increasing attention from researchers (Consoli et al., 2007; Dos Santos et al., 2010; Yetimoglu and Salbas, 2003). However, with the increasing demand for environmental protection, granular materials are being mixed with waste materials, including polyethylene (PE) fibers, polyvinyl chloride (PVC) fibers and tire-derived fibers, which have a low stiffness, as an environmental and economic practice in railway engineering applications (Fathali et al., 2017).

Therefore, the parameters of PE fibers, PVC fibers and rubber fibers are calibrated by performing the MTS EM tension test (as shown in Fig. 4 (a)). The elastic moduli (the secant moduli are considered as 2% axial strain) are approximately 1.13×10^8, $1.02 \times 10^7 Pa$ and $3.25 \times 10^6 Pa$ for the PE fibers, PVC fibers and rubber fibers, respectively, as shown in Fig. 4(b). According to the properties of the fiber materials shown in Table 2, the stiffness values of the fibers, 1×10^5,1×10^6, 1×10^7, and $1 \times 10^8 Pa$, are adopted, which are in the range of the stiffness values of several commonly used fiber materials. The stiffness determined by the calibration is the overall stiffness. Considering that the simplified parallel bond model is used for the fiber in this study (see Section 3.1 for details), the stiffness of the parallel bond model is calibrated through numerical tensile testing. The simulation process of the tensile testing is as follows. (1) The top and bottom of a fiber are bonded to walls with a

Table 1
Library of several particle shapes.

Digital	Contour	Elongation	Roundness	Roughness
1		0.8219	0.7510	0.00160
2		0.5576	0.5839	0.00129
3		0.6286	0.7043	0.00155
4		0.8907	0.682	0.00129
5		0.5749	0.5778	0.00111
6		0.7503	0.6324	0.00111
7		0.5135	0.5345	0.00115
8		0.9277	0.7575	0.00142
9		0.8464	0.6942	0.00147
10		0.8600	0.6734	0.00124

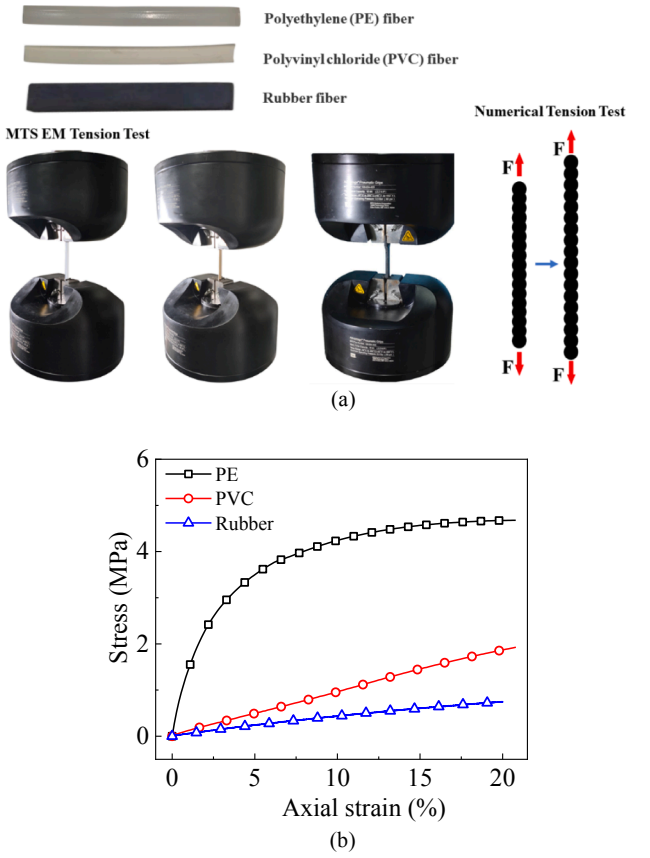

Fig. 4. Calibration of different fibers: (a) test materials and calibration and (b) test results of the MTS EM tension test.

high bond stiffness (1000 times the ball bond stiffness), and a constant velocity is applied to the top wall. (2) When the target strain is reached, the top wall is fixed until the unbalanced force ratio $< 10^{-10}$. (3) The tensile stress is recorded according to the contact force of the walls. The stiffnesses of the parallel bond model are presented in Table 3.

Table 2
Mechanical properties of common fibers.

Fiber material	Tensile strength (MPa)	Elastic modulus (MPa)
PE fiber	143.5	113.4
PVC fiber	–	10.20
Rubber fiber	30.0	3.25
Poroelastic materials (Lin et al., 2008)	–	less than1

Table 3
Samples of numerical simulation.

Sample name	Fiber content (%)	Fiber stiffness (Pa)	Parallel bond normal stiffness (Pa)
K0C00	0	–	–
K5C05	5	1×10^5	6.7×10^7
K5C10	10		
K5C15	15		
K6C05	5	1×10^6	6.7×10^8
K6C05	10		
K6C05	15		
K7C05	5	1×10^7	6.7×10^9
K7C05	10		
K7C05	15		
K8C05	5	1×10^8	6.7×10^{10}
K8C05	10		
K8C15	15		

3. DEM simulation

PFC2d5.0, a reliable numerical tool used to study granular materials with real shapes from a microscopic perspective (Liu et al., 2017), is used to perform the simulation in this study. Considering the particle shape and flexible boundary, 16 groups of FSMs are subjected to numerical biaxial tests. To simplify the expression of tests under different conditions, K5C15 denotes the test with a fiber stiffness of 1×10^5 and a FC of 15%, and K5 denotes the test with a fiber stiffness of 1×10^5. All the samples and their abbreviations are presented in Table 3.

3.1. Selection of contact models

In the numerical biaxial test performed on fiber-reinforced soil by considering a flexible boundary, two contact models are involved, including the linear elastic model and linear parallel bond model.

It has been proven that the linear elastic contact model exhibits realistic behaviors of multisphere-based (e.g., clump and cluster) granular materials (Gong et al., 2019; Zhao et al., 2020). Moreover, the operation of the linear elastic contact model is stable and efficient (Gong et al., 2019); thus, the linear elastic contact model is adopted to simulate the interactions between different objects, including soil–soil, soil–fiber,

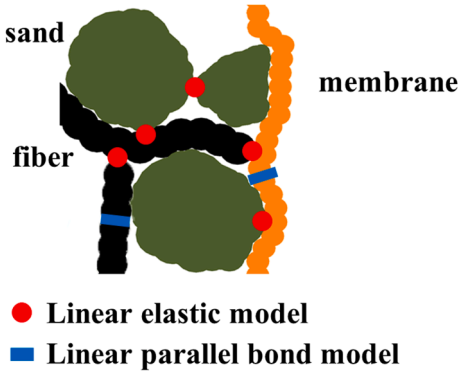

Fig. 5. Assignment of the contact model.

and fiber–fiber and the sample boundaries (as shown in Fig. 5). In this model, the contacts cannot resist the bending moment and tensile force and ultimately undergo linear elastic deformation and slide under compression. The force–displacement relationship can be expressed as follows:

$$F_n = k_n \mu_n \tag{4}$$

$$F_s = \begin{cases} k_s \mu_s & k_s \mu_s < u F_n \\ u F_n & k_s \mu_s > u F_n \end{cases} \tag{5}$$

where F, μ and k are the contact force, contact displacement and linear contact stiffness, respectively. The subscripts n and s indicate the normal and tangential directions, respectively, and u is the friction coefficient.

According to the suggestion proposed by Zhang (Zhang et al., 2020a), deformable agglomerates (clusters) are employed to simulate the fibers and membrane. Similar to fibers, the membrane is composed of a certain number of bonded particles with the same diameter (0.5 mm, equal to the thickness of the membrane) according to the simplified linear parallel bond model (Zhang et al., 2020a). The force and moment of the simplified linear parallel bond model are updated according to the following process. The bond force is decomposed into the normal force F_n and shear force F_s. In each time step of the simulation, the changes in these force and moment components are related to the relative motion of the particles as follows:

$$F_n = F_{n0} + \overline{k_n} A \Delta\delta_n \tag{6}$$

$$F_s = F_{s0} + \overline{k_s} A \Delta\delta_s \tag{7}$$

$$M_b = M_{b0} - \overline{k_n} I \Delta\theta_b \tag{8}$$

where F_{n0}, F_{s0} and M_{b0} denote the normal contact force, shear contact force, and bending moment, respectively, at the beginning of the time step; A and I denote the area and moment of inertia, respectively; $\overline{k_n}$ and $\overline{k_s}$ denote the normal and shear stiffness, respectively; and $\Delta\delta_n$, $\Delta\delta_s$ and $\Delta\theta_b$ denote the relative normal and shear displacement increments and bend–rotation increment, respectively.

The model parameters used in this investigation are carefully selected. The densities of the soil and fibers, which do not considerably influence the shear behaviors under quasistatic conditions are selected as 2650 kg/m^3 and 770 kg/m^3, respectively (Gong et al., 2020; Nie et al., 2019). The normal stiffness of a soil particle is selected as 1×10^8 *Pa* (Gong et al., 2019; Yang et al., 2016), and thus, the soil particle can be regarded as rigid (Zhang et al., 2021). According to Goldenberg and Goldhirsch (2005), the normal-to-shear stiffness ratio of a soil particle should be selected in the range of 1.0–1.5, which can satisfy the theoretical model of the elastic sphere contact in the Cattaneo–Mindlin model (Fischer-Cripps, 2000). In this investigation, the normal-to-shear stiffness ratio of a soil particle is selected as 1.07, which is consistent with the experimental observation of soil (Simmons and Brace, 1965). The friction coefficient of the soil particles is selected as 0.25 according to the strict calibration of soil conducted by Lopera Perez et al. (2017a); (2017b;), and the friction coefficient of a fiber is selected as 1.0 according to Gong et al. (2020). The bond strength of the fibers and membrane are selected as 1×10^{10} *Pa* to prevent the fibers and membrane from breaking during shear (Zhang et al., 2021). All the adopted model parameters are shown in Table 4. In terms of the surface property inheritance, the linear stiffnesses $\overline{k_n}$ and $\overline{k_s}$ and friction coefficient u are inherited from the contacting pieces. The linear stiffnesses are inherited assuming that the stiffnesses of both pieces act in series, using the following formulas:

$$\frac{1}{k_n} = \frac{1}{k_n^{(1)}} + \frac{1}{k_n^{(2)}} \tag{9}$$

Table 4
Parameters used in the DEM simulation.

Parameter	Value
Density of a soil particle (kg/m^3)	2650
Normal stiffness of a soil particle (Pa)	1×10^8
Normal-to-shear stiffness ratio of a soil particle	1.25
Friction coefficient of a soil particle	0.25
Density of a fiber particle (kg/m^3)	770
Effective modulus of a fiber particle (Pa)	See Table 1
Normal-to-shear stiffness ratio of a fiber particle	1.25
Parallel bond normal stiffness of a fiber particle (Pa)	See Table 1
Parallel bond stiffness ratio of a fiber particle	1.25
Tensile strength of a fiber particle (Pa)	1×10^{12}
Cohesion of a fiber particle (Pa)	1×10^{12}
Friction coefficient of a fiber particle	0.8
Damping coefficient	0.7

$$\frac{1}{k_s} = \frac{1}{k_s^{(1)}} + \frac{1}{k_s^{(2)}} \tag{10}$$

where (1) and (2) denote the properties of pieces 1 and 2, respectively.

Note that when the local distortion of the rubber membrane is large, new contacts are formed between the non-neighboring bonded particles. In this case, the linear elastic model is employed as the contact law to simulate the interaction between the non-neighboring bonded particles, which are denoted as membrane–membrane contacts. In addition, considering the initial overlap of the bonded particles, the density of the bonded particles is 650 kg/m^3 based on the real density of a rubber membrane (1100 kg/m^3).

3.2. Application of confining pressure

The confining pressure in the simulation is applied through a flexible membrane to maintain the stress homogeneity (Zhang et al., 2020a). As shown in Fig. 6, a cluster-based membrane is established using a series of bonded particles. The process of establishing the membrane is as follows:

(1) The distance between two adjacent adhesive particles on the flexible membrane is determined. To prevent the cluster-based flexible membrane from being punctured during servo and loading, the particles should have a certain amount of initial overlap. In this study, the distance between the centers of two bonded particles is set as 0.72 times the particle diameter (membrane thickness).

(2) Bonded particles are created according to the position of the walls after wall packing. The sample is surrounded by four rigid walls, including two loading walls and two sidewalls. The membrane is generated from one end of the sidewall to ensure a certain amount of overlap (0.36 times the particle diameter) between the first particle and wall. Next, the particles are generated according to the distance between the particle center until the distance between the last particle and the other end wall is less than the particle radius. After its generation, the simplified parallel bond model is assigned to the contact between each pair of adjacent bonded particles. In addition, to simulate the end restraint of the sample, the top and base bonded particles are fixed to the adjacent loaded walls, i.e., the particle velocity is equal to the wall velocity.

(3) Finally, the sidewalls are deleted, and the confining pressure is applied by exerting an external force on the bonded particles.

After generating the membrane, the confining pressure is applied to each particle unit through external forces according to the deformation of the membrane. Theoretically, the force acting on the particle element is the product of the confining pressure and equivalent area. In addition, the applied force is perpendicular to the equivalent area and points to the interior of the specimen. In the considered case, f_i^{eq} can be expressed

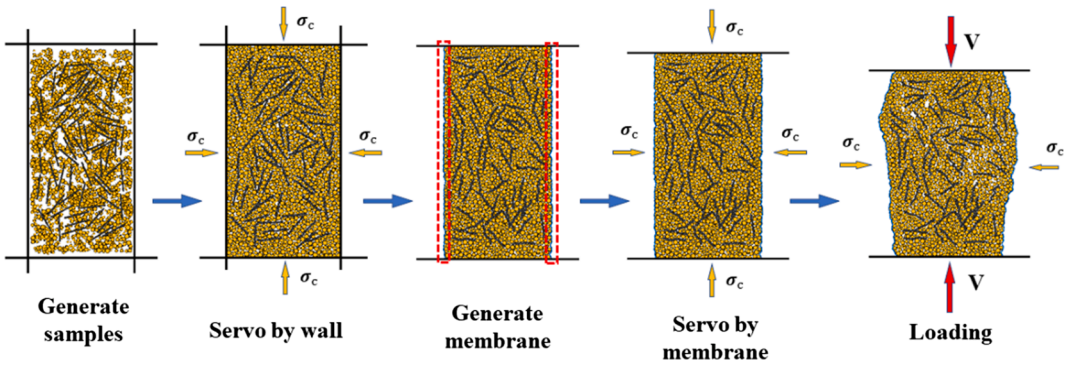

Fig. 6. Simulation process.

as follows:

$$f_i^{eq} = \sum (\frac{\sigma_c d_{ij}}{2}) \boldsymbol{n}_{ij} \tag{11}$$

where σ_c is the confining pressure, d_{ij} is the distance between two adjacent particles i and$j$, and $\boldsymbol{n}_{ij}$ is the normal unit vector perpendicular to line l_{ij}.

3.3. Simulation process

Referring to the values of the FC in the test and simulation (Eldesouky et al., 2016; Liu et al., 2018), we conducted biaxial compression tests on the four groups of fiber-reinforced soils with different fiber volume contents (0% 5% 10% 15%). The simulation process is shown in Fig. 6. The detailed simulation process is as follows:

(1) Sample generation. Four walls, e.g., two loading walls and two sidewalls, are generated with designed aspect ratios (height to width of 2:1). Next, the particle templates are selected randomly from the particle shape library. Nonoverlapping particles and fibers are randomly generated with random rotation angles in the container. The sample with the least number of particles contains 5276 particles. In this stage, the fibers are generated as clumps (agglomerates with deformation) to ensure that the fiber does not deform during the compaction process. The stiffness is set as 1×10^8 for all materials, and the friction coefficient of the contact is temporarily set as zero to ensure that the materials are completely dispersed (Gong and Liu, 2017).

(2) Wall packing. To ensure that the box shape is almost unchanged, the loading walls move toward the center of the container at a speed V_c (0.1 times the height of the sample (Gong and Liu, 2015)), and the sidewalls move at a speed $V_c/2$. This process is continued until the measured confining pressure is 0.8 times the designed confining pressure (50 kPa). Subsequently, pebbles (base particles in a clump) in a clump-based fiber are replaced with balls to generate a fiber. The contact inside the fiber is set as a parallel bond model, and the corresponding parameters are assigned. Subsequently, according to the traditional wall servo mechanism, the components are compressed isotopically (Gong and Liu, 2017). The isotropic compression continues until the ratio of the unbalanced force (ratio of the average unbalanced force to the average contact force (Farhang and Mirghasemi, 2017)) is less than 10^{-6}, and the deviation between the wall stress and confining stress is less than 0.1 kPa.

(3) Membrane packing. To eliminate the influence of initial randomness, the stiffness of the fiber is changed to the target stiffness to enable variable control of the stiffness. Next, the wall is replaced using a flexible membrane, and the confining pressure is again applied to the servo through the membrane.

(4) Shearing. After the membrane packing, the actual friction coefficient is applied to the granular system. The loading walls move toward each other at a shear strain rate ε, and the confining pressure is continuously applied to the flexible membrane according to Eq. (11). The shear process is continues until the axial strain reaches 15%. Note that the gravity is set as zero in this simulation to easily identify the stress transformation (Gong and Liu, 2015).

To ensure that the specimen remains in the quasistatic state, the shear strain rate should be sufficiently low such that the kinetic energy supplied by shearing is negligible compared with the static pressure. This aspect can be formulated in terms of an inertia parameter, I, defined as follows (Da Cruz et al., 2005):

$$I = \frac{\varepsilon \overline{D}}{\sqrt{p^{'}/\rho}} \tag{12}$$

where ε is the shear strain rate. Quasistatic shear is ensured by using a small I value in the granular system. Certain researchers recommended that I should be less than 2.5×10^{-3} or 1.0×10^{-3} (Agnolin and Roux, 2008; Lopera Perez et al., 2016); thus, the maximum shear strain rate is less than 0.05. Accordingly, I is less than 1.0×10^{-4} during shear.

Moreover, in the early stage of shearing, to reduce the influence of inertia on the measured stress data, the loading plates move at a low speed. After 1.0×10^5 cycles, the shear strain rate, ε, reaches a constant value. The value of ε can be expressed as follows:

$$\varepsilon = \begin{cases} 5N_{\Delta t}/10^6 N_{\Delta t} \le 10^4 \\ 0.05 N_{\Delta t} > 10^4 \end{cases} \tag{13}$$

where $N_{\Delta t}$ is the current number of cycles.

4. Simulation results and analyses

4.1. Macroscopic analyses

4.1.1. Stress and volumetric strain

The macroscale stress tensor used for the microscale quantities of the contact forces and contact vectors is as follows (Christoffersen et al., 1981):

$$\sigma_{ij} = \frac{1}{V} \sum_{c=1}^{N_c} f_i^c d_j^c \tag{14}$$

where V is the sample volume, c indicates a specific contact, N_c represents the contact number in the sample, f^c denotes the corresponding contact force, and d^c denotes the corresponding branch vector joining the centers of the two particles in contact. The effective mean ($p^{'}$) and deviatoric (q) stresses are defined as follows:

$$p^{'} = \frac{\sigma_1 + \sigma_2}{2} \tag{15}$$

$$q = \frac{\sigma_1 - \sigma_2}{2} \tag{16}$$

$$\eta = \frac{q}{p'} \tag{17}$$

where σ_1 and σ_2 indicate the axial stress and lateral stress, respectively. η is the stress ratio. The axial strain, ε_1, and volumetric strain, ε_v, are estimated from the boundary movements:

$$\varepsilon_1 = \frac{h_0 - h}{h_0} \tag{18}$$

$$\varepsilon_v = \frac{v_0 - v}{v_0} \tag{19}$$

where h_0 and h are the initial and current heights of the sample. v_0 is the initial volume of the sample, and v is the current volume of the sample. v can be calculated from the position of membrane particles. The membrane particles are initially ordered from top to bottom. Accordingly, the sample is divided into an m triangular mesh based on the sequential membrane particles. Thus, v is obtained by summing the area of the triangular mesh:

$$v = \sum \frac{1}{2} \left| (x_1 - x_0) \cdot (y_2 - y_0) - (x_2 - x_0) \cdot (y_1 - y_0) \right| \tag{20}$$

where (x_0, y_0), (x_1, y_1) and (x_2, y_2) are vertices of triangular elements.

Fig. 7 illustrates the stress ratio during shear with different fiber stiffnesses and contents. In general, the stress ratios first increase to a peak value and slowly decrease to a plateau. The curves change from strain softening to strain hardening as the fiber stiffness decreases. The addition of fibers leads to a reduction in the shear modulus of the sample, especially for the low-stiffness fiber. This phenomenon is consistent with that reported in previous investigations (Lopera Perez et al., 2017b; Zhang et al., 2021). For the sample with low-stiffness fibers (Fig. 7(a)), the axial strain corresponding to the peak stress ratio is remarkably delayed, which means that the toughness of the mixture increases. The effect of the reinforcement is consistent with that determined by a previous study on sand–rubber mixtures (Li et al., 2019). For fibers with high stiffness, the peak stress ratio and residual stress ratio increase considerably as the FC increases, consistent with the observation of sand–fiber (nylon wire) mixtures in laboratory tests (Sadek et al., 2010).

Fig. 8 displays the variation in the volumetric strain obtained with different fiber stiffnesses and contents. For all samples, the volumetric strain decreases until it reaches the minimum value, and this point is defined as the phase transformation state (Li and Wang, 1998). Subsequently, the samples begin to dilate. For the sample with a low fiber stiffness (Fig. 8(a)), the volume shrinkage increases with increasing FC, and the axial strain corresponding to the phase transformation state increases. The shear dilatancy in the residual state of fiber-reinforced soil is notably less than that of the unreinforced samples. For the sample with high-stiffness fibers (Fig. 8(b)), the addition of fibers promotes dilatancy. This phenomenon indicates that the samples with low-stiffness fibers are denser than those with high-stiffness fibers after shear. The increasing FC leads to an increase in the effect of the fibers.

4.1.2. Shear strength and dilatancy

The internal friction angle, φ, which represents the shear strength of the granular material, can be defined by the stress ratio in biaxial loading based on the Mohr–Coulomb criterion:

$$\sin\varphi = \frac{\sigma_1 - \sigma_2}{\sigma_1 + \sigma_2} = \frac{q}{p'} \tag{21}$$

Moreover, to quantify the effect of fibers on the degree of dilatancy, the dilatancy angle, which is equal to the instantaneous movement angle of a sliding block relative to the fracture surface (Schanz and Vermeer, 1996; Yin et al., 2018), is adopted to quantify the degree of dilatancy. In biaxial loading, the dilatancy angle can be written as follows:

$$\psi = \arcsin \frac{\frac{d\varepsilon_v}{d\varepsilon_1}}{\frac{d\varepsilon_v}{d\varepsilon_1} - 2} \tag{22}$$

Fig. 9(a) shows the variation in the peak friction angle (φ_p) and residual friction angle (φ_r) of the samples. φ_p increases as the fiber stiffness increases. Compared with samples with low FC, the gap of φ_p is larger at a high FC. This phenomenon can also be attributed to the increase in the FC increasing the effect of fibers. φ_r increases as the fiber stiffness increases. The results show that fibers with high stiffness can play a greater role in the reinforcement of soil. Interestingly, there exists a threshold fiber stiffness, which is 1×10^7 in this study. As the FC increases, the φ_p value of the samples with high-stiffness fibers (fibers with stiffness values larger than the threshold) increases, and this trend is opposite to that for the samples with low-stiffness fibers. Moreover, all the φ_r values increase as FC increases.

Fig. 9(b) illustrates the correlation between the maximum dilatancy angle and FC under different fiber stiffnesses. As the fiber stiffness increases, the maximum dilatancy angle increases. When the stiffness is less than the threshold, the maximum dilatancy angle increases as the FC decreases. This phenomenon indicates that fibers with low stiffness (fibers with stiffness values less than the threshold) inhibit dilation. When the fiber stiffness is larger than the threshold, the addition of fibers promotes the dilatancy of the samples, and the promotion effect increases as the FC increases.

The widely used empirical stress–dilatancy relationship that focuses on the strength parameters of uniform sand, developed by Bolton (1986), indicates that:

$$\varphi_p = \varphi_c + a\psi_p \tag{23}$$

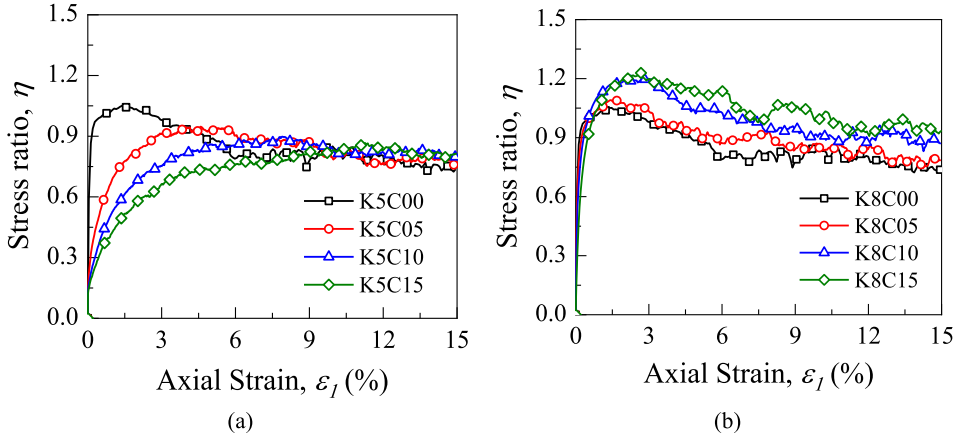

Fig. 7. Stress–strain relationship for samples with fiber stiffness values of (a) K5 and (b) K8.

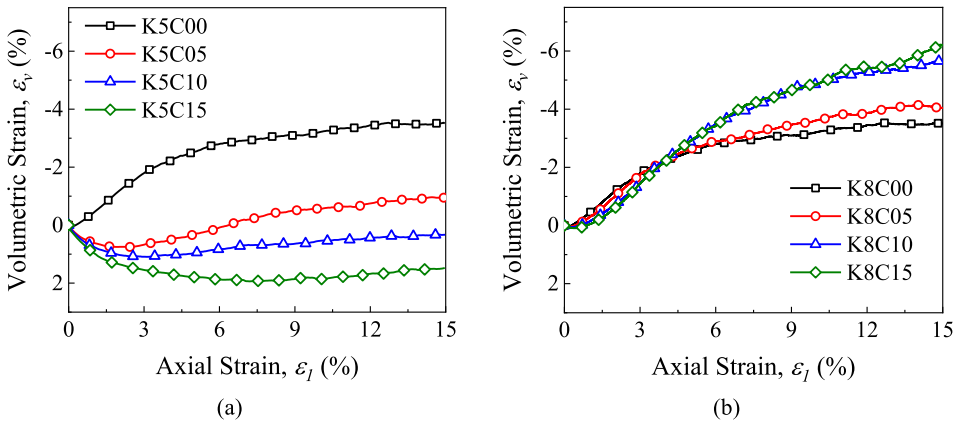

Fig. 8. Volumetric strain for samples with fiber stiffness values of (a) K5 and (b) K8.

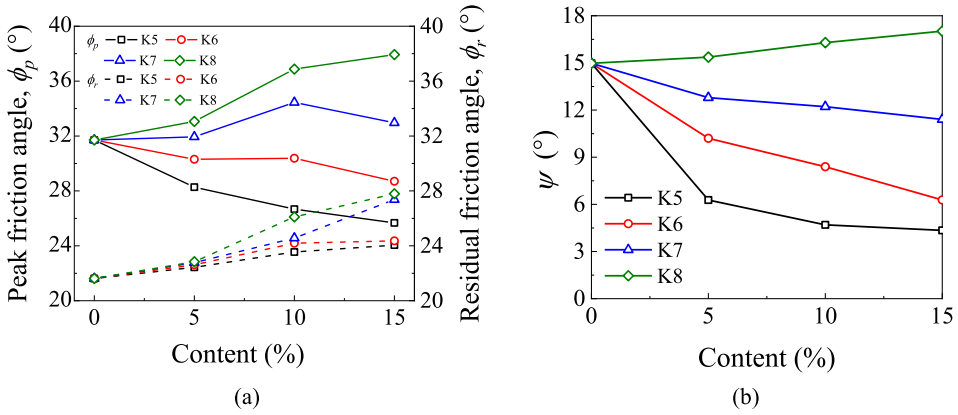

Fig. 9. (a) Internal friction angle and (b) maximum dilatancy angle.

where the dilatancy coefficient, a, represents the contribution of the dilatancy to the peak-state strength and varies based on the soil type. Bolton (1986) suggested that $a = 0.48$ in the triaxial compression condition for clean sand. In this investigation, the stress–strain curve is basically stable when the axial strain reaches 15%, and thus, the residual value of the internal friction angle is used to express the critical value.

Fig. 10 illustrates the evolution of a with different fiber stiffnesses and FCs. The φ_p of fiber-reinforced soil can be expressed using equation (23). Furthermore, this law was observed in previous laboratory tests of sand–polyethylene terephthalate (PET) mixtures performed by Shariatmadari et al. (2020). Compared with the pure sand test conducted by Guo and Su (2007), the value of a in this study is between that of angular sand and rounded sand. This finding indicates that the addition of fibers exerts only a small influence on the stress–dilatancy relationship. According to Figs. 8 and 9, as the fiber stiffness increases at a certain FC, increasing φ_p can increase both φ_r and ψ_p. When the fiber stiffness is less than the threshold, φ_p decreases with FC because the increasing φ_r values cannot compensate for the decreasing ψ_p values. When the stiffness is greater than the threshold, both φ_r and ψ_p increase with FC, which leads to an increase in φ_p.

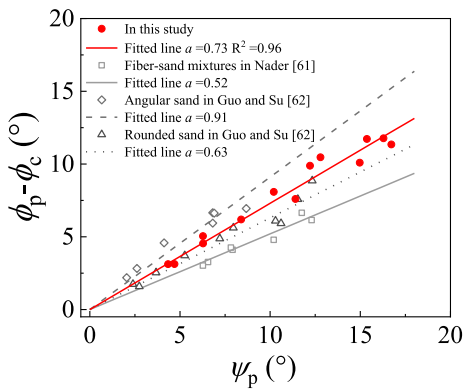

Fig. 10. Stress–dilatancy relationship.

4.2. Microscopic quantities

The microscopic behaviors of the fiber-reinforced soil are investigated through a series of microscopic indexes, including the mobilization of the fiber internal force, average coordination number, connectivity, contribution of the different contacts and sliding percentage.

4.2.1. Visualization of numerical samples

The contact forces considerably contribute to the shear strength (Zhao and Zhou, 2017). To intuitively understand the physical mechanism of a particle system during the shear process, it is necessary to visualize the contact force networks (Nie et al., 2019). Fig. 11 shows the contact force networks of samples with different FCs and fiber stiffnesses at the initial and residual states. The line thickness in Fig. 11 is proportional to the magnitude of the contact force. In the initial states, the contact forces in the vertical and horizontal directions are nearly equal in magnitude. At the residual states, the value of the contact forces considerably increases. The contact forces of the sample with low-stiffness fibers (K5C15) show weaker anisotropy and lower magnitude

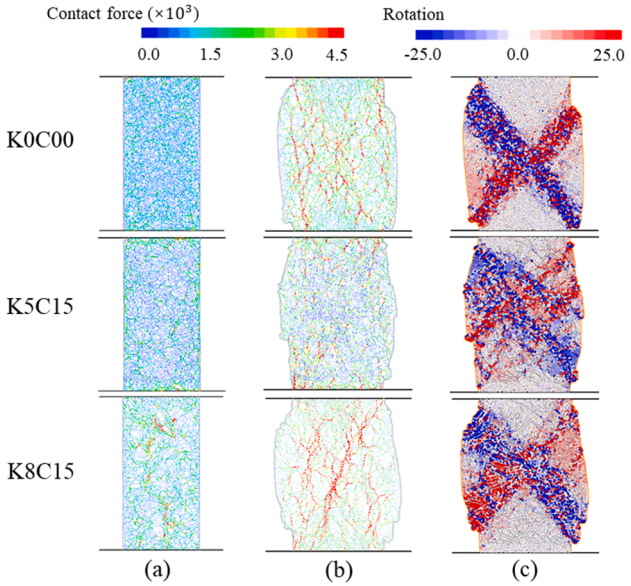

Fig. 11. Visualization of numerical samples: (a) contact force in the initial state, (b) contact force in the residual state and (c) rotation of particles.

than the pure particle sample. In contrast, for the sample with high-stiffness fibers (K8C15), the contact forces close to the vertical direction are considerably higher in magnitude, exhibiting a notable anisotropy compared to the sample with the pure particles. This phenomenon indicates that the addition of fibers with low stiffness results in a uniform stress network during shear.

The shear band of the soils is a key phenomenon of failure in granular systems. The rotation of particles is a convenient and effective way of highlighting the shear band (Zhu and Yin, 2019). As shown in Fig. 11, the pure soil sample and sample with high-stiffness fibers exhibit notable shear bands, while the shear bands in the sample with low-stiffness fibers are not as distinct. This finding indicates that the addition of fibers with a low stiffness leads to the formation of uniform internal structures of the samples during shear.

4.2.2. Contribution of the different contacts

The contribution, C_k, of specific contact types k can help explain the change in the mixture skeleton (Li et al., 2019) and quantify the effect of different contact types on the resistance to the external load. According to Gong and Liu (2017), the contribution of different contacts to the shear strength can be expressed as follows:

$$C_k = \frac{q_k/p}{q/p} = \frac{\sigma_1^k - \sigma_3^k}{\sigma_1 - \sigma_3} \times 100\% \tag{24}$$

Fig. 12 illustrates the contribution of each contact type to the shear strength during shearing. As the axial strain increases, the contribution of the soil–soil contact, C_{SS}, gradually decreases to a plateau. This phenomenon indicates that fibers gradually play a greater role during shear. In this case, C_{FF} increases and C_{SS} decreases as the fiber stiffness increases. Moreover, C_{SF} increases in this period, indicating that the interface between the fiber and soil becomes increasingly notable as the fiber stiffness increases. Interestingly, in the case of samples with high-stiffness fibers (with a stiffness larger than the threshold), C_{SS} first increases slightly and later gradually decreases to a plateau, indicating that the reinforcement mechanism changes as the fiber stiffness increases. As the FC increases, C_{FF} and C_{SF} increase while C_{SS} decreases. In summary, as the fiber stiffness and content increase, the skeleton of fiber-reinforced soil changes from a soil skeleton to a coupled bearing framework.

4.2.3. Mobilization of the fiber internal force

The strength improvement of fiber-reinforced granular materials largely depends on the potential mobilization of internal forces in the fibers (Gong et al., 2020). Considering the nonuniform stress within the fiber and lack of indexes to quantify the state of the fiber, two simple indexes are proposed to quantitatively describe the current status of the fibers, including the normalized average tensile force, A_T, and ratio of the tension to the compression force, R_{TC}. A_T describes the mobilization degree of the fiber internal force, and R_{TC} describes the type of fiber internal force (tension or compression).

Fig. 13 (a) illustrates the variation in A_T during shear. A_T increases and later plateaus as the axial strain increases, and the A_T of high-stiffness fibers is larger than that of low-stiffness fibers. The results illustrate that the fibers are gradually activated, and the reinforcement is more significant during shear. This finding is consistent with the numerical investigation of fiber-reinforced sand (Gong et al., 2020). The evolution of R_{TC} with axial strain is illustrated in Fig. 13(b). R_{TC} is less than 1 at first, indicating that the fiber is easily compressed during packing. Next, R_{TC} gradually increases and becomes stable. Compared with that of high-stiffness fibers, the R_{TC} of low-stiffness fibers increases faster during shear, and the value of R_{TC} is larger than 1.0 in the residual state. This finding indicates that the low-stiffness fibers reinforce the soil by providing tension, and the reinforcement achieved using high-stiffness fibers is based on compression. Furthermore, the R_{TC} of high-stiffness fibers stabilizes sooner than that of low-stiffness fibers, indicating that the reinforcement achieved with high-stiffness fibers is easier to mobilize.

Fig. 13(c) shows the values of A_T and R_{TC} in the residual state. A_T increases rapidly as the fiber stiffness increases. In the case of low-

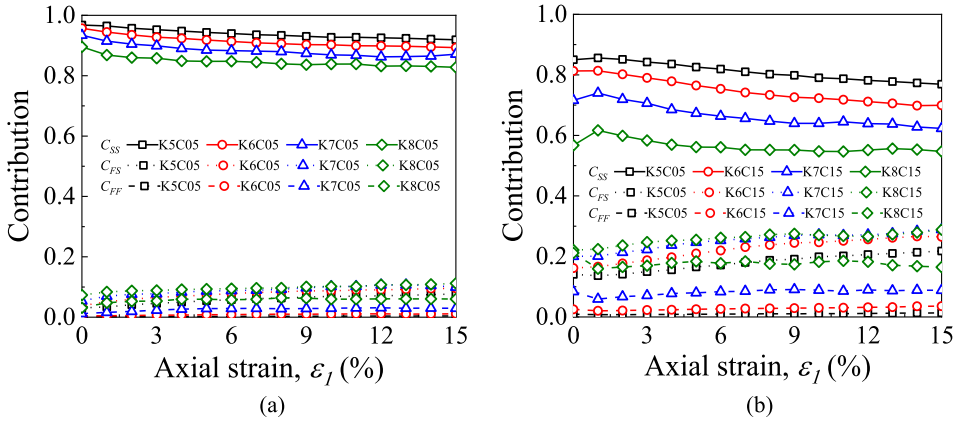

Fig. 12. Contribution of the different contact types for samples with fiber content values of (a) the C05 and (b) C15.

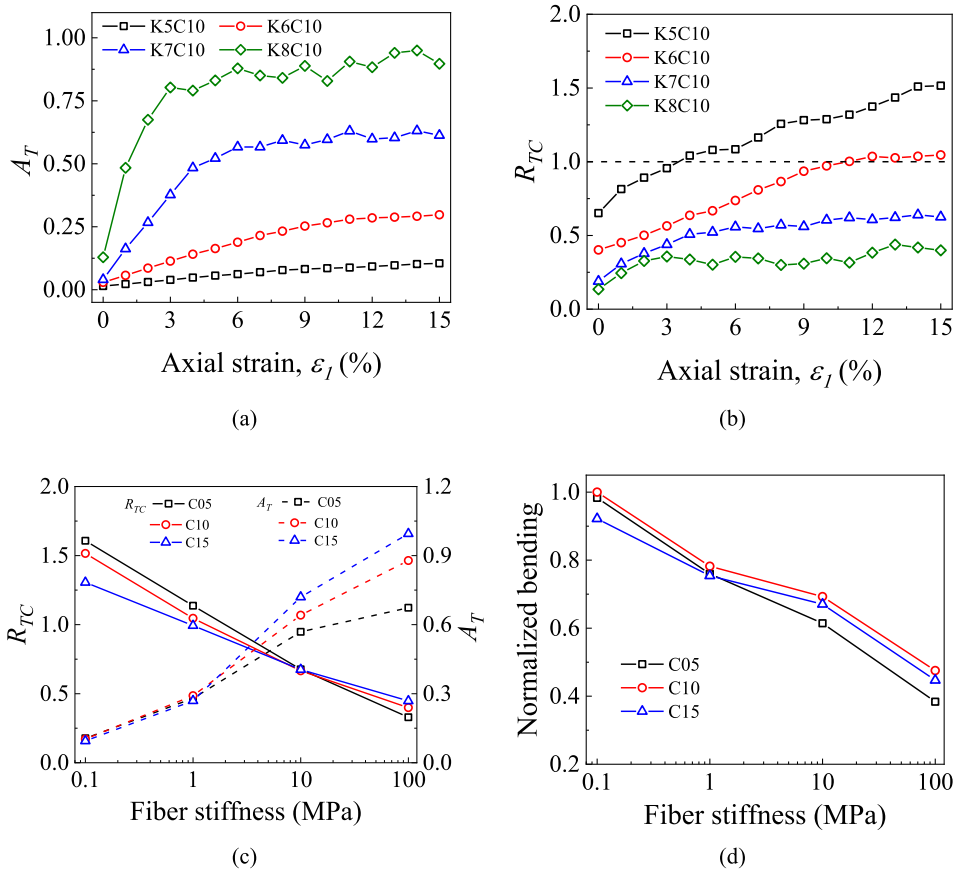

Fig. 13. Mobilization of the fiber internal force: (a) A_T in the residual state, (b)R_{TC} in the residual state, (c) evolution of R_{TC} and A_T with the fiber stiffness and (d) evolution of the normalized bending of the fibers with the fiber stiffness.

stiffness fibers, A_T is not sensitive to the change in FC. However, for high-stiffness fibers, FC tends to promote A_T. These findings indicate that the high-stiffness fibers more easily interact with one another than the low-stiffness fibers. Moreover, R_{TC} decreases as the stiffness increases. Interestingly, the threshold of the stiffness found in terms of the strength and dilatation also appears in microbehavioral states. When the stiffness equals K7 (threshold of the stiffness in this study), R_{TC} values with different FCs intersect at one point.

To analyze the deformation of the fibers more clearly, the bending degree is quantified, as shown in Fig. 13 (d). The fiber is composed of balls; thus, the bending degree of a fiber is calculated by summing the angle between the branch vector of the adjacent balls and principal direction of the fiber. The principal direction of a fiber is defined as the line with the minimum moment of inertia. The bending degree of the fibers is significantly reduced as the fiber stiffness increases. This result indicates that the reinforcement mechanism of the high-stiffness fibers pertains to the structure; in other words, the high-stiffness fibers bear the bending moment and support the surrounding particles. Consequently, the support leads to the local loosening of the surrounding particles and dilatancy of the samples.

4.2.4. Coordination number

The coordination number, Z (defined as the average number of neighboring objects for a specific object), which is highly related to the rearrangement of particles, is an essential index used to investigate the internal structure of mixtures (Rothenburg and Kruyt, 2004). According to Gong et al. (2019), the coordination number is related to the contact type. Under the investigated conditions, the number of fibers is small; thus, the shown coordination number includes the coordination number of particle–particle contact, Z_{ss}, and coordination number of fiber–soil particle contact, Z_{fs}, as follows:

$$Z_{ss} = \frac{2N_c^{SS}}{N_S} \tag{25}$$

$$Z_{fs} = \frac{2N_c^{FS}}{N_F} \tag{26}$$

where N_c^{SS} is the total number of soil particles around the soil particles, N_S is the number of soil particles, N_F is the number of fibers, and N_c^{FS} is the number of soil particles around the soil particles.

Fig. 14 illustrates the coordination number of the particle–particle contact Z_{ss}. For the sample with low-stiffness fibers, Z_{ss} remains basically stable during shear, indicating that the rearrangement of the particles around low-stiffness fibers is rare, and the area surrounding the fibers is always dense during shear. This phenomenon leads to the restraint of the dilatancy when low-stiffness fibers are added to granular systems. For the sample with high-stiffness fibers, Z_{ss} decreases rapidly to a plateau with increasing strain, which indicates that the soil particles are redistributed in the early stage of loading and later stabilize. Z_{ss} in the residual state decreases as the fiber stiffness increases, which indicates that the presence of fibers with a higher stiffness loosens the residual state of the sample, which is consistent with the phenomenon observed in the volumetric strain curve.

As shown in Fig. 15(a), in the case of low fiber stiffness (less than the threshold), Z_{fs} first increases to a peak and later stabilizes with shearing. This phenomenon indicates that Z_{fs} is sensitive to the local stress in the presence of low-stiffness fibers. In the case of high fiber stiffness (larger than the threshold), Z_{fs} exhibits a notable decrease during shear, indicating that the content of local voids around the high-stiffness fibers gradually increases. Fig. 15(b) shows the variation in Z_{fs} with different stiffnesses and FCs in the residual state. Z_{fs} decreases as the fiber stiffness

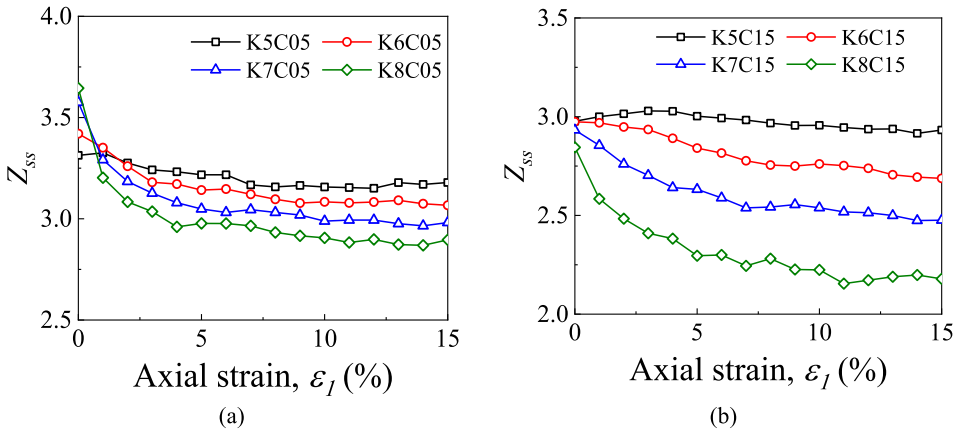

Fig. 14. Coordination numbers Z_{ss} for a fiber content of (a) C05 and (b) C15.

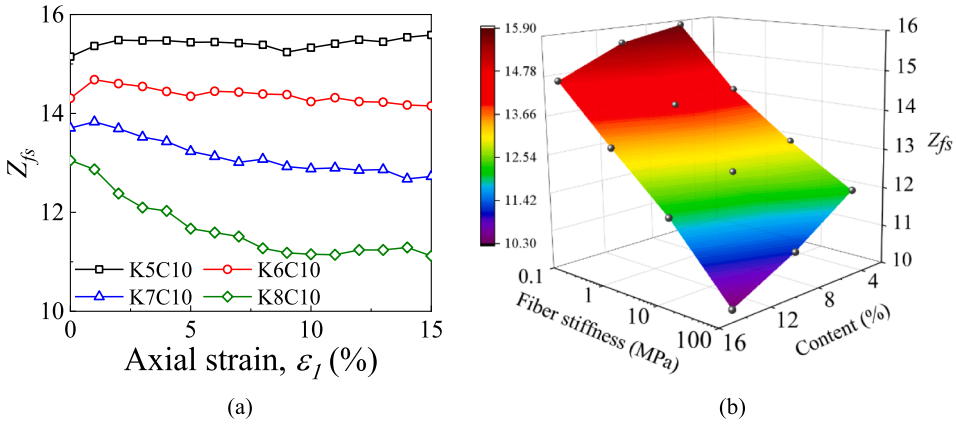

Fig. 15. Coordination numbers Z_{fs}: (a)Z_{fs} with fiber content C10 and (b) Z_{fs} in the residual state.

and content increases. This finding indicates that low-stiffness fibers deform more easily and fill the surrounding void; thus, the fiber contacts more soil particles. Furthermore, unlike in the 3D condition (Zhang et al., 2021), the fibers affect one another in the internal structure in 2D space, even if the FC is low (volume content of less than 10%).

4.2.5. Connectivity

The connectivity, C, is the contact number of a given particle. The percentage of particles with connectivity C ≥ 3 under the 2D condition, P(C ≥ 3), can reflect the proportion of particles that contribute to the external load (Zhang et al., 2020b).

Fig. 16(a) displays the evolution of P(C ≥ 3) against the axial strain. For the sample with low-stiffness (less than the threshold) fibers, P(C ≥ 3) remains nearly constant during shear. However, for the sample with high-stiffness fibers (larger than the threshold), P(C ≥ 3) decreases rapidly to a stable value. Fig. 16(b) displays the evolution of P(C ≥ 3) against the fiber stiffness at different FCs. As the fiber stiffness increases, P(C ≥ 3) gradually decreases. When the fiber stiffness reaches a certain threshold (K7 in this study), the P(C ≥ 3) value of the samples with different FCs intersects at a point. At this time, the change in the FC does not affect the stability of the sample. This finding indicates that the threshold of the fiber stiffness is the turning point of the stability of the

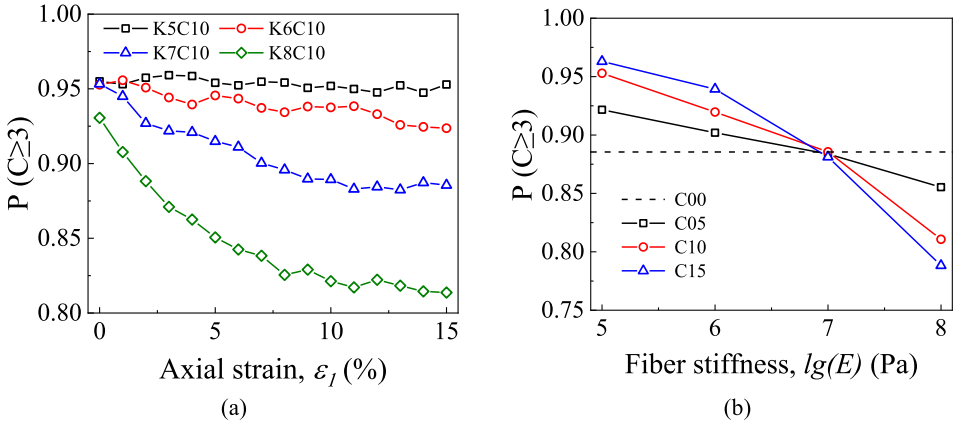

Fig. 16. Evolution of P(C ≥ 3) (a) with shear and (b) against the fiber stiffness at different FCs.

sample. The addition of fibers with high stiffness (larger than the threshold) decreases the internal stability of the samples, and low-stiffness fibers lead to the opposite trend. This finding can be explained as follows. Low-stiffness fibers are easy to stretch and penetrate, resulting in larger contact areas with rigid particles. In contrast, high-stiffness fibers support surrounding particles during shear, leading to a loose local structure. In addition, the effect of the stability from the fibers becomes more notable as the FC increases. This finding can be confirmed by the variation in the internal force in the fibers.

4.2.6. Sliding

The sliding contact can be used to explain the limitation imposed by the fibers on the particles (Liu et al., 2018). Therefore, the percentage of sliding contacts of type k is considered to investigate the interaction between different objects. The percentage of sliding contacts of type k (S_k) can be defined as follows:

$$S_k = \frac{N_s^k}{N_k} \tag{27}$$

where N_s^k is the number of sliding contacts of type k calculated according to the Coulomb friction law. The soil particles are divided into surrounding particles (particles in contact with fibers) and non-surrounding particles (particles not in contact with fibers). Thus, $S_{P(S)}$ denotes the sliding ratio between the surrounding and non–surrounding particles, and $S_{P(N)}$ denotes the sliding ratio between two non–surrounding particles. Moreover, S_P is the sliding ratio of particles, including both surrounding and non–surrounding particles.

Fig. 17 (a) shows the percentage of sliding contact during shear at 10% FC. S_P first increases rapidly to a peak value. The peak value increases as the fiber stiffness increases, especially when the fiber stiffness is lower than the threshold. Next, S_P decreases and stabilizes. After an axial strain of 10% is attained, the influence of the fiber stiffness on S_P is not notable. To explore the influence of high-friction fiber–particle interfaces with different fiber stiffnesses, $S_{P(S)}$ and $S_{P(N)}$ are analyzed. For the low-stiffness fiber, as shown in Fig. 17(b), $S_{P(S)}$ is always larger than $S_{P(N)}$. This finding indicates that low-stiffness fibers limit the motion of surrounding particles due to the high-friction fiber–particle interfaces. This restriction is transferred to the interior of the particles. However, in the case of high fiber stiffness, the gap between $S_{P(S)}$ and $S_{P(N)}$ is exceedingly small, as shown in Fig. 17(c). This finding indicates that the high-stiffness fiber directly supports the surrounding particles because of the high bending capacity, which weakens the high-friction interface.

5. Conclusion

To quantitatively analyze the effects of fiber stiffness and FC on the shear behaviors of fiber-reinforced soils, a series of numerical biaxial compression tests are conducted considering the real particle shape and flexible boundary. The results are analyzed from both macro- and microstate perspectives. A threshold value of the fiber stiffness (corresponding to K7) is determined, which leads to the different reinforcement mechanisms of fibers. The main conclusions can be summarized as follows:

1) The addition of fibers with large friction coefficients increases the residual strength of the samples. The addition of high-stiffness (larger than the threshold) fibers leads to an increase in the peak strength and dilatancy of the mixtures. The low-stiffness (less than the threshold) fibers have the opposite effect. Increasing FC only enhances the effect of the fiber. In addition, the peak friction angle of fiber-reinforced soil has a linear relationship with the peak dilatancy

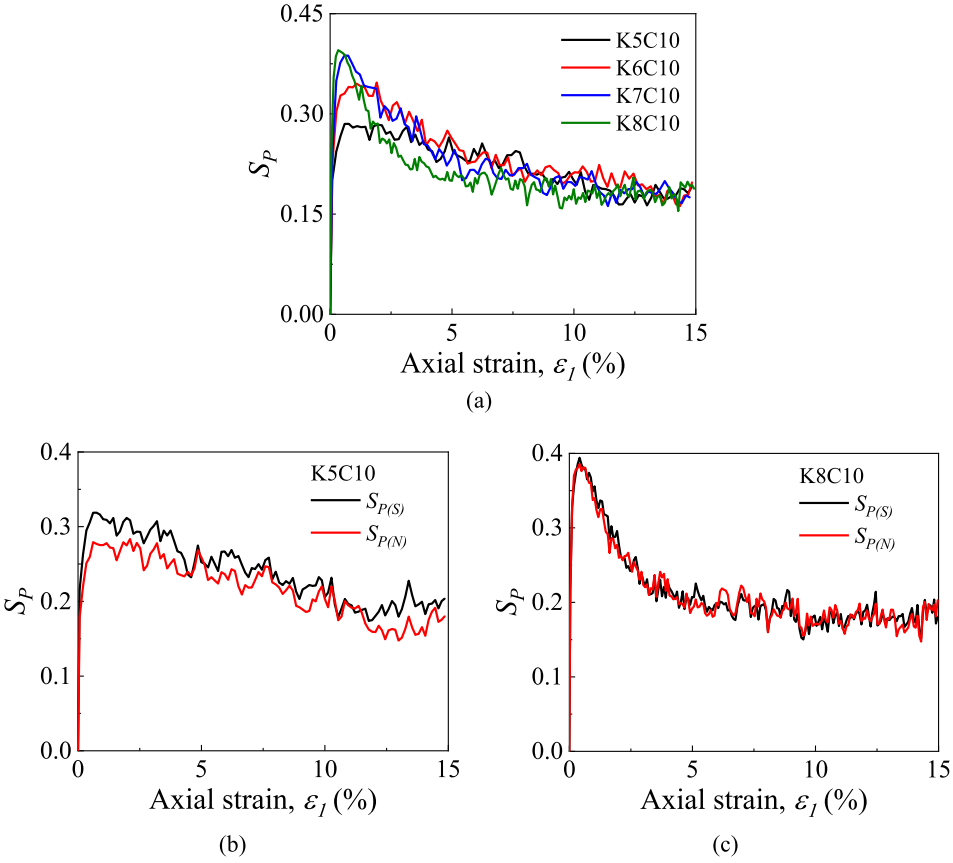

Fig. 17. Sliding ratio: (a) percentage of the sliding contact with shear, (b) evolution of $S_{P(S)}$ and $S_{P(N)}$ of sample K5C10 with shear and (c) evolution of $S_{P(S)}$ and $S_{P(N)}$ of sample K8C10 with shear.

angle, and the addition of fibers has only a slight effect on the stress–dilatancy relationship.

2) In terms of the microscopic properties of mixtures, the low-stiffness (less than the threshold) fibers effectively enhance the internal stability of the samples and ratio of tensile contact in the fiber; in contrast, the high-stiffness fibers have adverse effects. When the fiber stiffness approaches the threshold, the internal stability of the samples remains basically unchanged as the FC increases, and the ratio of the tensile contact inside the fibers remains constant.
3) As the fiber stiffness increases, the resistance of fibers to external forces increases, and the soil skeleton changes to a fiber–soil joint skeleton. Low-stiffness fibers are flexible and deformable; in this configuration, the higher surface friction of the fiber restrains the shear dilatancy. The high-stiffness fibers can resist bending, thereby directly supporting the surrounding particles, and the effect of the high surface friction is not notable.

CRediT authorship contribution statement

Ningyu Yang: Writing - original draft, Methodology, Software, Conceptualization. **Xiaobin Chen:** Writing - review & editing, Funding acquisition, Resources, Validation. **Ruidong Li:** Software, Data curation, Visualization. **Junqi Zhang:** Writing - review & editing, Conceptualization. **Hang Hu:** Investigation, Data curation, Visualization. **Jiasheng Zhang:** Supervision, Project administration.

Declaration of Competing Interest

The authors declare that they have no known competing financial interests or personal relationships that could have appeared to influence the work reported in this paper.

Acknowledgments

The study was supported by the National Natural Science Foundation of China under grant number CNNSF 51978674. The authors appreciate this financial assistance.

References

Agnolin, I., Roux, J.N., 2008. On the elastic moduli of three-dimensional assemblies of spheres: Characterization and modeling of fluctuations in the particle displacement and rotation. Int. J. Solids Struct. 45 https://doi.org/10.1016/j.ijsolstr.2007.07.016.
Ajayi, O., Le Pen, L., Zervos, A., Powrie, W., 2017. A behavioural framework for fibre-reinforced gravel. Geotechnique 67. https://doi.org/10.1680/jgeot.16.P.023.
Akbarimehr, D., Eslami, A., Aflaki, E., 2020. Geotechnical behaviour of clay soil mixed with rubber waste. J. Clean. Prod. 271 https://doi.org/10.1016/j.jclepro.2020.122632.
Al-Refeai, T.O., 1991. Behavior of granular soils reinforced with discrete randomly oriented inclusions. Geotext. Geomembranes 10. https://doi.org/10.1016/0266-1144(91)90009-L.
Bolton, M.D., 1986. The strength and dilatancy of sands. Geotechnique 36. https://doi.org/10.1680/geot.1986.36.1.65.
Botero, E., Ossa, A., Sherwell, G., Ovando-Shelley, E., 2015. Stress-strain behavior of a silty soil reinforced with polyethylene terephthalate (PET). Geotext. Geomembranes 43. https://doi.org/10.1016/j.geotexmem.2015.04.003.
Christoffersen, J., Mehrabadi, M.M., Nemat-Nasser, S., 1981. A micromechanical description of granular material behavior. J. Appl. Mech. Trans. ASME 48. https://doi.org/10.1115/1.3157619.
Consoli, N.C., Casagrande, M.D.T., Coop, M.R., 2007. Performance of a fibre-reinforced sand at large shear strains. Geotechnique 57. https://doi.org/10.1680/geot.2007.57.9.751.
Da Cruz, F., Emam, S., Prochnow, M., Roux, J.N., Chevoir, F., 2005. Rheophysics of dense granular materials: Discrete simulation of plane shear flows. Phys. Rev. E - Stat. Nonlinear, Soft Matter Phys. 72 https://doi.org/10.1103/PhysRevE.72.021309.
Diambra, A., Ibraim, E., Russell, A.R., Muir Wood, D., 2013. Fibre reinforced sands: From experiments to modelling and beyond. Int. J. Numer. Anal. Methods Geomech. 37 https://doi.org/10.1002/nag.2142.
Dos Santos, A.P.S., Consoli, N.C., Baudet, B.A., 2010. The mechanics of fibre-reinforced sand. Geotechnique 60. https://doi.org/10.1680/geot.8.P.159.
Eldesouky, H.M., Morsy, M.M., Mansour, M.F., 2016. Fiber-reinforced sand strength and dilation characteristics. Ain Shams Eng. J. 7 https://doi.org/10.1016/j.asej.2015.06.003.
Farhang, B., Mirghasemi, A.A., 2017. A study of principle stress rotation on granular soils using DEM simulation of hollow cylinder test. Adv. Powder Technol. 28 https://doi.org/10.1016/j.apt.2017.05.011.
Fathali, M., Nejad, F.M., Esmaeili, M., 2017. Influence of Tire-Derived Aggregates on the Properties of Railway Ballast Material. J. Mater. Civ. Eng. 29 https://doi.org/10.1061/(asce)mt.1943-5533.0001702.
Fischer-Cripps, A.C., 2000. Introduction to Contact Mechanics. Introduction to Contact Mechanics. https://doi.org/10.1007/b97709.
Goldenberg, C., Goldhirsch, I., 2005. Friction enhances elasticity in granular solids. Nature 435. https://doi.org/10.1038/nature03497.
Gong, J., Liu, J., 2017. Effect of aspect ratio on triaxial compression of multi-sphere ellipsoid assemblies simulated using a discrete element method. Particuology 32. https://doi.org/10.1016/j.partic.2016.07.007.
Gong, J., Liu, J., 2015. Analysis on the mechanical behaviors of soil-rock mixtures using discrete element method, in: Procedia Engineering. https://doi.org/10.1016/j.proeng.2015.01.315.
Gong, J., Nie, Z., Zhu, Y., Liang, Z., Wang, X., 2019. Exploring the effects of particle shape and content of fines on the shear behavior of sand-fines mixtures via the DEM. Comput. Geotech. 106 https://doi.org/10.1016/j.compgeo.2018.10.021.
Gong, L., Nie, L., Liu, C., Xu, Y., 2020. Modelling Triaxial Tests on Fibre-Reinforced Sands with Different Fibre Orientations Using the Discrete Element Method. KSCE J. Civ. Eng. 24 https://doi.org/10.1007/s12205-020-1050-x.
Gray, D.H., Al-Refeai, T., 1986. Behavior of fabric-versus fiber-reinforced sand. J. Geotech. Eng. 112 https://doi.org/10.1061/(ASCE)0733-9410(1986)112:8(804).
Guo, P., Su, X., 2007. Shear strength, interparticle locking, and dilatancy of granular materials. Can. Geotech. J. 44 https://doi.org/10.1139/T07-010.
Islam, S.M.S., Bennamoun, M., Davies, R., 2008. Fast and fully automatic ear detection using cascaded adaboost, in: 2008 IEEE Workshop on Applications of Computer Vision, WACV. https://doi.org/10.1109/WACV.2008.4544023.
Jamshidi Chenari, R., Karimpour Fard, M., Pourghaffar Maghfarati, S., Pishgar, F., Lemos MacHado, S., 2016. An investigation on the geotechnical properties of sand-EPS mixture using large oedometer apparatus. Constr. Build. Mater. 113 https://doi.org/10.1016/j.conbuildmat.2016.03.083.
Jiang, M., Yin, Z.Y., 2014. Influence of soil conditioning on ground deformation during longitudinal tunneling. Comptes Rendus - Mec. https://doi.org/10.1016/j.crme.2014.02.002.
Jin, Y.F., Yin, Z.Y., Shen, S.L., Hicher, P.Y., 2016. Investigation into MOGA for identifying parameters of a critical-state-based sand model and parameters correlation by factor analysis. Acta Geotech. 11 https://doi.org/10.1007/s11440-015-0425-5.
Jin, Y.F., Yin, Z.Y., Shen, S.L., Zhang, D.M., 2017. A new hybrid real-coded genetic algorithm and its application to parameters identification of soils. Inverse Probl. Sci. Eng. 25 https://doi.org/10.1080/17415977.2016.1259315.
Jin, Y.F., Yin, Z.Y., Wu, Z.X., Daouadji, A., 2018. Numerical modeling of pile penetration in silica sands considering the effect of grain breakage. Finite Elem. Anal. Des. 144 https://doi.org/10.1016/j.finel.2018.02.003.
Li, W., Kwok, C.Y., Sandeep, C.S., Senetakis, K., 2019. Sand type effect on the behaviour of sand-granulated rubber mixtures: Integrated study from micro- to macro-scales. Powder Technol. 342 https://doi.org/10.1016/j.powtec.2018.10.025.
Li, X.S., Wang, Y., 1998. Linear Representation of Steady-State Line for Sand. J. Geotech. Geoenvironmental Eng. 124 https://doi.org/10.1061/(asce)1090-0241(1998)124:12(1215).
Lin, Y.L., Wang, D.M., Lu, W.M., Lin, Y.S., Tung, K.L., 2008. Compression and deformation of soft spherical particles. Chem. Eng. Sci. 63 https://doi.org/10.1016/j.ces.2007.09.028.
Ling H I, T.F., 1994. Performance of anisotropic geosynthetic-reinforced cohesive soil mass. J. Geotech. Eng.
Liu, J., Bai, Y., Song, Z., Wang, Y., Chen, Z., Wang, Q., Kanungo, D.P., Qian, W., 2018. Effect of basalt fiber on the strength properties of polymer reinforced sand. Fibers Polym. 19 https://doi.org/10.1007/s12221-018-8507-2.
Liu, Y., Zhou, X., You, Z., Yao, S., Gong, F., Wang, H., 2017. Discrete element modeling of realistic particle shapes in stone-based mixtures through MATLAB-based imaging process. Constr. Build. Mater. 143 https://doi.org/10.1016/j.conbuildmat.2017.03.037.
Lopera Perez, J.C., Kwok, C.Y., O'Sullivan, C., Huang, X., Hanley, K.J., 2016. Assessing the quasi-static conditions for shearing in granular media within the critical state soil mechanics framework. Soils Found. 56 https://doi.org/10.1016/j.sandf.2016.01.013.
Lopera Perez, J.C., Kwok, C.Y., Senetakis, K., 2017a. Investigation of the micro-mechanics of sand–rubber mixtures at very small strains. Geosynth. Int. 24 https://doi.org/10.1680/jgein.16.00013.
Lopera Perez, J.C., Kwok, C.Y., Senetakis, K., 2017b. Effect of rubber content on the unstable behaviour of sand–rubber mixtures under static loading: a micro-mechanical study. Géotechnique. https://doi.org/10.1680/jgeot.16.p.149.
Michalowski, R.L., Čermák, J., 2003. Triaxial compression of sand reinforced with fibers. J. Geotech. Geoenvironmental Eng. 129 https://doi.org/10.1061/(asce)1090-0241(2003)129:2(125).
Naderi, E., Hataf, N., 2014. Model testing and numerical investigation of interference effect of closely spaced ring and circular footings on reinforced sand. Geotext. Geomembranes 42. https://doi.org/10.1016/j.geotexmem.2013.12.010.
Nie, Z., Zhu, Y., Wang, X., Gong, J., 2019. Investigating the effects of Fourier-based particle shape on the shear behaviors of rockfill material via DEM. Granul. Matter 21. https://doi.org/10.1007/s10035-019-0875-9.
Patel, S.K., Singh, B., 2019. Shear strength response of glass fibre-reinforced sand with varying compacted relative density. Int. J. Geotech. Eng. 13 https://doi.org/10.1080/19386362.2017.1352157.

Qu, T., Feng, Y.T., Wang, Y., Wang, M., 2019. Discrete element modelling of flexible membrane boundaries for triaxial tests. Comput. Geotech. 115 https://doi.org/10.1016/j.compgeo.2019.103154.

Rothenburg, L., Kruyt, N.P., 2004. Critical state and evolution of coordination number in simulated granular materials. Int. J. Solids Struct. 41 https://doi.org/10.1016/j.ijsolstr.2004.06.001.

Sadek, S., Najjar, S.S., Freiha, F., 2010. Shear strength of fiber-reinforced sands. J. Geotech. Geoenvironmental Eng. 136 https://doi.org/10.1061/(asce)gt.1943-5606.0000235.

Santoni, R.L., Tingle, J.S., Webster, S.L., 2001. Engineering properties of sand-fiber mixtures for road construction. J. Geotech. Geoenvironmental Eng. 127 https://doi.org/10.1061/(asce)1090-0241(2001)127:3(258).

Schanz, T., Vermeer, P.A., 1996. Angles of friction and dilatancy of sand. Geotechnique 46. https://doi.org/10.1680/geot.1996.46.1.145.

Shariatmadari, N., Karimpour-Fard, M., Hasanzadehshooiili, H., Hoseinzadeh, S., Karimzadeh, Z., 2020. Effects of drainage condition on the stress-strain behavior and pore pressure buildup of sand-PET mixtures. Constr. Build. Mater. 233 https://doi.org/10.1016/j.conbuildmat.2019.117295.

Sharma, V., Kumar, A., 2019. Numerical study of ring and circular foundations resting on fibre-reinforced soil. Int. J. Geotech. Eng. https://doi.org/10.1080/19386362.2019.1603680.

Simmons, G., Brace, W.F., 1965. Comparison of static and dynamic measurements of compressibility of rocks. J. Geophys. Res. 70 https://doi.org/10.1029/jz070i022p05649.

Viola P, J.M., 2001. Robust Real-time Object Detection. Robust Real-time Object Detect.

Wang, L., Zhu, B., Li, J.C., Chen, Y.M., 2014. Two-phase constitutive model for fiber-reinforced soil. Yantu Gongcheng Xuebao/Chinese J. Geotech. Eng. 36. https://doi.org/10.11779/CJGE201407017.

Wang, P., Karatza, Z., Arson, C., 2019. DEM modelling of sequential fragmentation of zeolite granules under oedometric compression based on XCT observations. Powder Technol. 347 https://doi.org/10.1016/j.powtec.2019.02.050.

Wang, P., Yin, Z.Y., 2020. Micro-mechanical analysis of caisson foundation in sand using DEM. Ocean Eng. 203 https://doi.org/10.1016/j.oceaneng.2020.107240.

Wang, X., Nie, Z., Gong, J., Liang, Z., 2021. Random generation of convex aggregates for DEM study of particle shape effect. Constr. Build. Mater. 268 https://doi.org/10.1016/j.conbuildmat.2020.121468.

Yang, Y., Wang, J.F., Cheng, Y.M., 2016. Quantified evaluation of particle shape effects from micro-to-macro scales for non-convex grains. Particuology 25. https://doi.org/10.1016/j.partic.2015.01.008.

Yetimoglu, T., Salbas, O., 2003. A study on shear strength of sands reinforced with randomly distributed discrete fibers. Geotext. Geomembranes 21. https://doi.org/10.1016/S0266-1144(03)00003-7.

Yin, Z.-Y., Wu, Z.-X., Hicher, P.-Y., 2018. Modeling Monotonic and Cyclic Behavior of Granular Materials by Exponential Constitutive Function. J. Eng. Mech. 144 https://doi.org/10.1061/(asce)em.1943-7889.0001437.

Yin, Z.Y., Wang, P., Zhang, F., 2020. Effect of particle shape on the progressive failure of shield tunnel face in granular soils by coupled FDM-DEM method. Tunn. Undergr. Sp. Technol. 100 https://doi.org/10.1016/j.tust.2020.103394.

Zhang, J., Wang, X., Yin, Z.Y., Liang, Z., 2020a. DEM modeling of large-scale triaxial test of rock clasts considering realistic particle shapes and flexible membrane boundary. Eng. Geol. 279 https://doi.org/10.1016/j.enggeo.2020.105871.

Zhang, Junqi, Chen, X., Zhang, Jiasheng, Jitsangiam, P., Wang, X., 2021. DEM investigation of macro- and micro-mechanical properties of rigid-grain and soft-chip mixtures. Particuology 55. https://doi.org/10.1016/j.partic.2020.06.002.

Zhang, Junqi, Chen, X., Zhang, Jiasheng, Wang, X., 2020b. Microscopic investigation of the packing features of soft-rigid particle mixtures using the discrete element method. Adv. Powder Technol. 31 https://doi.org/10.1016/j.apt.2020.05.019.

Zhao, L., Zhang, S., Huang, D., Wang, X., 2020. A digitalized 2D particle database for statistical shape analysis and discrete modeling of rock aggregate. Constr. Build. Mater. 247 https://doi.org/10.1016/j.conbuildmat.2019.117906.

Zhao, S., Zhou, X., 2017. Effects of particle asphericity on the macro- and micro-mechanical behaviors of granular assemblies. Granul. Matter 19. https://doi.org/10.1007/s10035-017-0725-6.

Zhu, H.-X., Yin, Z.-Y., 2019. Grain Rotation-Based Analysis Method for Shear Band. J. Eng. Mech. 145 https://doi.org/10.1061/(asce)em.1943-7889.0001654.